

# An energy-preserving level set method for multiphase flows

N. Valle<sup>a</sup>, F.X. Trias<sup>a</sup>, J. Castro<sup>a</sup>

<sup>a</sup>*Heat and Mass Transfer Technological Centre (CTTC), Universitat Politècnica de Catalunya - BarcelonaTech (UPC), ESEIAAT, Carrer Colom 11, 08222 Terrassa (Barcelona)*

---

## Abstract

The computation of multiphase flows presents a subtle energetic equilibrium between potential (i.e., surface) and kinetic energies. The use of traditional interface-capturing schemes provides no control over such a dynamic balance. In the spirit of the well-known symmetry-preserving and mimetic schemes, whose physics-compatible discretizations rely upon preserving the underlying mathematical structures of the space, we identify the corresponding structure and propose a new discretization strategy for curvature. The new scheme ensures conservation of mechanical energy (i.e., surface plus kinetic) up to temporal integration. Inviscid numerical simulations are performed to show the robustness of such a method.

*Keywords:* Multiphase Flow, Symmetry-preserving, Mimetic, Conservative Level Set, Energy-preserving

---

## 1. Introduction

Multiphase flows are ubiquitous in industrial applications. They are present in a rich variety of physical phenomena such as vaporization [1], atomization [2], electrohydrodynamics [3] or boiling [4], among others [5, 6].

The use of interface-capturing schemes is widespread for the computation of multiphase flows due to its computational efficiency. The Volume-Of-Fluid (VOF) by Hirt and Nichols [7], the Level Set method developed by Osher and Sethian [8] and most recently phase field methods, introduced by Anderson et al. [9], are the most popular

---

\*Corresponding author

*Email addresses:* nicolas.valle@upc.edu (N. Valle), xavi@cttc.upc.edu (F.X. Trias), jesus@cttc.upc.edu (J. Castro)

interface capturing schemes for multiphase flows. An overview of these can be found in [10] and references therein. Despite the pros and cons that each method presents, we made our development concrete on the Conservative Level Set (CLS) initially developed by Olsson and Kreiss [11] and Olsson et al. [12] due to its good conservation properties, curvature accuracy and ease of handling topological changes. This was extended to unstructured collocated meshes in [13].

Of particular interest are the incompressible Navier-Stokes equations,

$$\rho \left( \frac{\partial \vec{u}}{\partial t} + (\vec{u} \cdot \nabla) \vec{u} \right) = \nabla \cdot \sigma \quad \nabla \cdot \vec{u} = 0 \quad (1)$$

where the stress tensor  $\sigma$  is composed of the hydrostatic and the deviatoric ones ( $\sigma = -p\mathbb{I} + \tau$ ). In turn,  $\tau$  is defined by Stokes constitutive equation  $\tau = 2\mu S$ , while the strain tensor is given by  $S = 1/2(\nabla \vec{u} + (\nabla \vec{u})^T)$ .

The proper solution of equations (1) requires an appropriate decoupling of pressure and velocity. In this regard, the Fractional Step Method (FSM) [14] is an excellent tool which properly enforces the incompressibility constraint. However, the FSM results in a Poisson equation which needs to be solved, which takes most of the computational time in a typical simulation.

The construction of discrete differential operators in the seminal work of Versteappen and Veldman [15, 16] aims at preserving physical quantities of interest, namely momentum and kinetic energy, by preserving several mathematical properties at the discrete level. This merges with the conception of mimetic finite difference methods [17], where the discretization is performed to satisfy the inherent mathematical structure of the space, naturally producing a physics-compatible discretization. The present work is motivated by such an appealing idea. This has been named mimetic [17] or discrete vector calculus [18], among others [19, 20]. Mimetic methods delve into the construction of discrete differential operators by producing discrete counterparts of more fundamental mathematical concepts, making extensive use of exterior calculus. This approach results in the algebraic concatenation of elementary operators, namely matrices and vectors. Such an approach can be seen as the mathematical dual of the physics-motivated work on symmetry-preserving schemes and provides with a different point of view which fortifies the analysis of this family of methods, which have

been used in both academic [21] and industrial problems [22, 23], among others. However, to our knowledge, there is no a straightforward extension of these ideas into the multiphase flow community yet.

While Direct Numerical Simulation (DNS) of single-phase flows has reached substantial maturity, multiphase flows lag behind due to its increased complexity, namely due to two main issues: *i*) surface tension and *ii*) differences in physical properties. The former results in a dynamic equilibrium between kinetic and potential energies, which are exchanged through the capillary term. Indeed this is the reason why symmetry-preserving discretizations [15, 16], despite conserving flawlessly kinetic (and thus total) energy in single-phase flows, do not suffice to preserve mechanical energy in multiphase flows, as this transfer needs to be taken into account explicitly. The latter poses challenges regarding how interpolations need to be done without breaking physical laws. In the framework of VOF, Fuster [24] proposed a discretization that preserves the (skew-)symmetries of the momentum equation, preserving kinetic energy up to surface tension, which is regarded as an energy source. However, as far as surface tension is not included into the analysis, this is a necessary, but not a sufficient condition for preserving mechanical energy. Regarding the viscous term, the work of Sussman et al. [25] provided with a conservative discretization. The interested reader is referred to [26] and references therein for a comparison between different discretization strategies for the viscous term. Despite the impressive progress done so far, none of the above have included surface tension, and thus potential energy, in the analysis of conservation of energy. It is well-known, however, that the imbalances in the surface tension term may lead to spurious currents and, eventually, unstable solutions [27]. In the framework of phase field methods, the impact of surface tension on the energy balance has been included in the works of Jacqmin [28] for the Cahn-Hilliard equation, and Jamet et al. [29] and Jamet and Misbah [30] for the Allen-Cahn formulation. This paper aims to dig into a discretization including surface tension which, without recompression, preserves mechanical energy for level set schemes.

The rest of the paper is arranged as follows: in Section 2 a glimpse of algebraic topology is provided. This sets the foundations to review the well-known symmetry-preserving discretization for single-phase flows in Section 3 and, inspired by this, de-

velop a new energy-preserving scheme for multiphase flows in Section 4. Comparative results between current techniques and the newly developed methods are presented in Section 5. Finally, conclusions and future insights are outlined in Section 6.

## 2. Topological model

Any numerical approach requires a finite-dimensional representation of the spaces under consideration. This implies a discrete representation of the domains involved in the setup of the problem. Single-phase flows fit well into a fixed frame, typically discretized on a fixed grid. On the other hand, multiphase flows require to account for a moving interface which splits the domain at question into two regions. This interface needs to be properly discretized in order to preserve several inherent topological properties. The way this is accomplished has led to a diversity of multiphase methods [10].

### 2.1. Mesh

Let  $\Omega$  be the working domain bounded by  $\partial\Omega$  and assume that  $M$  is a partition of  $\Omega$  into a non-overlapping mesh. An illustrative example is given in Figure 1. Although we stick to structured meshes for computational simplicity, the formulation presented here is independent of the mesh structure and thus can be extended into unstructured meshes. Incidence matrices are used to account for the connectivity within geometric entities. An example for  $T_{FC}$ , the incidence matrix relating faces with cells according to the orientation of the mesh given in Figure 1 is shown next

$$T_{FC} = \begin{matrix} & f_1 & f_2 & f_3 & f_4 & f_5 & f_6 & f_7 & f_8 & f_9 & f_{10} & f_{11} & f_{12} \\ \begin{matrix} c_1 \\ c_2 \\ c_3 \\ c_4 \end{matrix} & \begin{pmatrix} -1 & -1 & 0 & +1 & 0 & +1 & 0 & 0 & 0 & 0 & 0 & 0 & 0 \\ 0 & 0 & -1 & -1 & +1 & 0 & 0 & +1 & -1 & 0 & 0 & 0 & 0 \\ 0 & 0 & 0 & 0 & 0 & -1 & -1 & 0 & +1 & 0 & +1 & 0 & 0 \\ 0 & 0 & 0 & 0 & 0 & 0 & 0 & -1 & -1 & +1 & 0 & +1 & 0 \end{pmatrix} \end{matrix} \quad (2)$$

They replace usual neighboring relations such as  $\phi_c = \sum_{f \in c} \phi_f$  for the sum of face values related to cell  $c$ . In addition, its transpose provides with an explicit form for

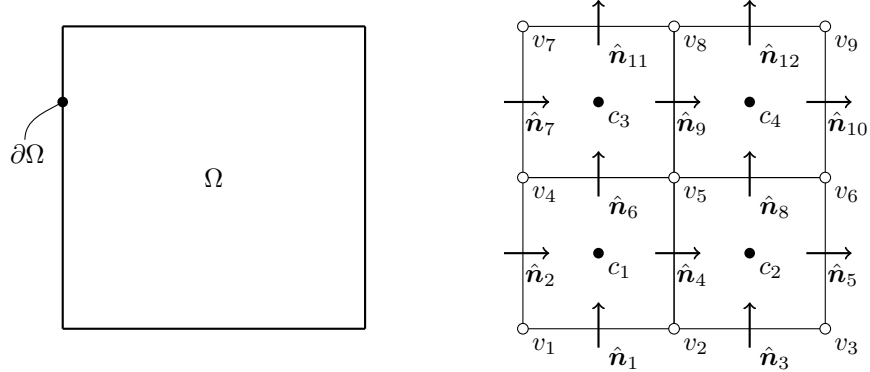


Figure 1: Left: Domain  $\Omega$  and its boundary  $\partial\Omega$ . Right: Mesh  $M$ .  $c_i$  corresponds with the  $i$ th cell,  $\hat{n}_i$  corresponds with the normal vector to the  $j$ th face (i.e.,  $f_j$ ) and  $v_k$  corresponds with the  $k$ th vertex. Its incidence matrix is stated in equation (2).

$\Delta_f \phi = \phi_+ - \phi_-$  for the difference across face  $f$ , among others. Basic geometric properties such as edge lengths ( $W_E$ ), face surfaces ( $A_F$ ) and cell volumes ( $V_C$ ) are arranged as diagonal matrices. This matrix perspective presents several advantages: *i*) mesh independence, *ii*) computational simplicity and *iii*) readily accessible algebraic analysis. While we restrain ourselves from digging into the first two, the later is useful both for reviewing the classical symmetry-preserving scheme and the development of the novel technique described here. Hereafter, lowercase letters correspond with vectors, whose subscript indicates the geometric entity to which they are linked (e.g.,  $p_c$  corresponds to pressure located at cells). Capital letters correspond with matrices, whose subscript(s) identify rows and (if different) columns (e.g.  $T_{FC}$  is the face-to-cell incidence matrix).

## 2.2. Interface

Interfaces imply a moving topology along the working domain, which implies a Lagrangian frame of reference. Interface tracking schemes track such a frame explicitly, at the expenses of numerical complexity [31]. On the other hand, interface capturing schemes preserve a fully Eulerian approach, by mapping quantities expressed in the Lagrangian frame back into the Eulerian one [7, 32, 33]. This results in a simpler implementation of the interface at the cost of an implicit representation. At this point

we split the presentation between the techniques used to actually capture the evolution of the interface and the ones used to obtain explicit geometric information out of the implicit form.

### 2.2.1. Interface Capturing

Let's assume now that the domain  $\Omega$  presents an interface at  $\Gamma$ , which splits  $\Omega$  into  $\Omega^+$  and  $\Omega^-$ . We note that the volume of a single phase  $\Omega^+$  can be defined as

$$\int_{\Omega^+} dV = \int_{\Omega} H(r) dV \quad (3)$$

where  $r$  corresponds with the signed shorter distance from an arbitrary point to the interface, as can be seen in Figure 2, while  $H(r)$  is its corresponding Heaviside step function, which is valued 1 at phase  $\Omega^+$  and 0 otherwise. Note that this function is the key to map a Lagrangian frame ( $\Omega^+$ ) back into an Eulerian one ( $\Omega$ ). Specific tracking of such a quantity is the basis of the Volume of Fluid (VOF) method [7], which yields to the concept of volume fraction or, more generally, marker function. Despite being formally neat, the implementation of specific convection schemes is required, eventually requiring full geometric reconstruction, resulting in an intricate implementation. A different approach is to capture the interface with a CLS [11, 12]. This captures the interface as the isosurface of a continuous and smooth function  $\theta$ . The level set marker function,  $\theta$ , results in a smoothed Heaviside step function that preserves  $\int_{\Omega} \theta dV = \int_{\Omega} H(r) dV$ . It is constructed as the convolution of the distance function  $r$  as follows

$$H(r) \approx \theta(r) = \frac{1}{2} \left( \tanh\left(\frac{r}{2\epsilon}\right) + 1 \right) \quad (4)$$

where  $\epsilon$  corresponds with a smoothing factor. Note that  $\theta(r) \rightarrow H(r)$  as  $\epsilon \rightarrow 0$ . Further details can be found in [13, 34].

By imposing the conservation of the marker function, we can advect such a marker in an incompressible flow as [11, 12, 13]:

$$\frac{\partial \theta}{\partial t} + (\vec{u} \cdot \nabla) \theta = 0 \quad (5)$$

where particular advection schemes and recompression stages can be added in order to obtain a sharper profile. The interested reader is referred to [11, 13] and references therein.

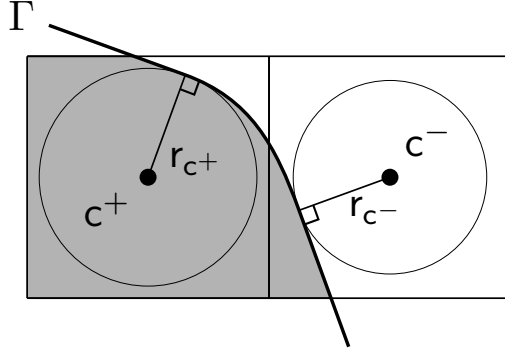


Figure 2: Distances  $r_{c^\pm}$  are defined as the shorter distances of the interface to the cell. These are then normal to the interface and correspond with the minimum radius of the tangent sphere.

### 2.2.2. Interface Reconstruction

Surface reconstruction may start by defining the interface normal. It is computed as [11]

$$\hat{\eta}_i = \frac{\nabla\theta}{|\nabla\theta|} \quad (6)$$

Which implies, by definition, that the gradient of the marker function  $\theta$  is parallel to the normal. On the other hand, curvature is computed as

$$\kappa = -\nabla \cdot \hat{\eta}_i \quad (7)$$

Now, the surface area of  $\Gamma$  can be computed in any of the following forms

$$A = \int_{\Gamma} dA = \int_{\Omega} \delta(r) dV = \int_{\Omega} \nabla H(r) \cdot \hat{\eta}_i dV \quad (8)$$

where  $\delta(r)$  is Dirac's delta function, which formally is the distributional derivative of the Heaviside step function. This is the basis of the celebrated continuum surface force of Brackbill et al. [35] for surface tension and, in general, of other smoothed interface methods. Regardless of the reconstruction method of choice, surface needs to satisfy first variation of area formula, which relates surface and volume variations through curvature and velocity as

$$\frac{d}{dt} \int_{\Gamma} dA = - \int_{\Gamma} \kappa \vec{u} \cdot \hat{\eta}_i dA \quad (9)$$

This is a fundamental identity, and the ultimate responsible of the correct conversion between kinetic and surface energy, as it will be shown in Section 4.1. A detailed

proof of this can be found in chapter 8.4 of Frankel [36]. As an illustrative example, let us consider the surface variation of a spherical surface. If we analyze how  $A = 4\pi r^2$  evolves under the action of the normal velocity,  $\dot{r}$ , we obtain that  $\frac{dA}{dt} = 8\pi r\dot{r}$ , which can be rearranged as  $\frac{dA}{dt} = \frac{2}{r}A\dot{r}$ , where we identify  $\kappa = \frac{2}{r}$ , the mean curvature of sphere. We are now going to prove that the use of a smooth marker function as in equation (4) leads to a consistent modeling of the interface by reconstructing surface area with its smooth counterpart  $\tilde{A}$  as

$$A \stackrel{(8)}{=} \int_{\Omega} \nabla H(r) \cdot \hat{\eta}_i dV \stackrel{(4)}{\approx} \int_{\Omega} \nabla \theta \cdot \hat{\eta}_i dV \stackrel{(6)}{=} \int_{\Omega} |\nabla \theta| dV = \tilde{A} \quad (10)$$

We now show that equation (10) is a compatible approximation of  $A$ . In particular, we prove that equation (9) is still valid when we replace  $A$  by  $\tilde{A}$ , which is defined over the volumes and thus much more convenient to compute. First, as a preliminary stage, we take the gradient of the transport equation (5) in the pursue of a relation between the marker function and the smoothed surface

$$\frac{\partial \nabla \theta}{\partial t} + \nabla((\vec{u} \cdot \nabla)\theta) = 0 \quad (11)$$

Finally, before moving on to the announced proof, let us introduce the inner product notation  $(\cdot, \cdot)$ , which simplifies bi-linear integrals as  $\int fg dS = (f, g)$ . In addition, concepts such as orthogonality, duality or (skew-)symmetry are naturally expressed in this framework. Further details can be found in Appendix A. With this in mind, we can proceed to approximate the left hand side of equation (9) via equation (10), to yield the following

$$\begin{aligned} \frac{d}{dt} \int_{\Gamma} dA &\stackrel{(10)}{\approx} \frac{d\tilde{A}}{dt} = \frac{d}{dt} (\nabla \theta, \hat{\eta}_i) = \left( \frac{d\nabla \theta}{dt}, \hat{\eta}_i \right) + \left( \nabla \theta, \frac{d\hat{\eta}_i}{dt} \right) \\ &= \left( \frac{\partial \nabla \theta}{\partial t}, \hat{\eta}_i \right) + \overbrace{\left( (\vec{u} \cdot \nabla) \nabla \theta, \hat{\eta}_i \right)} + \left( \nabla \theta, \frac{\partial \hat{\eta}_i}{\partial t} \right) + \overbrace{\left( \nabla \theta, (\vec{u} \cdot \nabla) \hat{\eta}_i \right)} \\ &= \left( \frac{\partial \nabla \theta}{\partial t}, \hat{\eta}_i \right) + \left( \nabla \theta, \frac{\partial \hat{\eta}_i}{\partial t} \right) \stackrel{(11)}{=} -(\nabla((\vec{u} \cdot \nabla)\theta), \hat{\eta}_i) \\ &= (\nabla \cdot \hat{\eta}_i, \vec{u} \cdot \nabla \theta) \quad \square \end{aligned} \quad (12)$$

where we exploit the skew-symmetry of the convective operator in the second row of eq. (12), benefit from  $\frac{\partial \hat{\eta}_i}{\partial t} \perp \nabla \theta$  in the third one and the duality between gradient and divergence in the last one.



Regarding the approximation of the right hand side of equation (9), we can proceed by including equation (7) and then using equation (10) to move from surface to volume integrals as

$$- \int_{\Gamma} \kappa \vec{u} \cdot \hat{\eta}_i dA \stackrel{(7)}{=} \int_{\Gamma} (\nabla \cdot \hat{\eta}_i) \vec{u} \cdot \hat{\eta}_i dA \stackrel{(10)}{\approx} (\nabla \cdot \hat{\eta}_i, \vec{u} \cdot \nabla \theta) \quad (13)$$

We finally obtain:

$$\frac{d}{dt} \int_{\Gamma} d\tilde{A} = ((\vec{u} \cdot \nabla) \theta, \nabla \cdot \hat{\eta}_i) = - \int_{\Gamma} \kappa \vec{u} \cdot \hat{\eta}_i dA \quad (14)$$

We conclude that, from a continuum point of view, the use of a marker function together with the surface reconstruction strategy stated in equation (10) results in a consistent capture of both the interface and its geometric features, namely the first variation of area equation (9). Notice that this analysis is not exclusive to level sets, but rather extensible to other interface capturing schemes as far as the surface can be cast into a potential form as in equation (10).

### 3. Symmetry-preserving discretization of single-phase flows

In an incompressible flow, in the absence of external forces, the net balance of mechanical energy is due to the viscous term of the Navier-Stokes equation solely. This is a relevant property for the simulation of turbulent flows, particularly for the computation of DNS. In this section, the well-known finite volume, staggered, symmetry-preserving discretization of Verstappen and Veldman [15, 16] is briefly reviewed. This sets the ground of the newly developed energy-preserving scheme presented in section 4. Assuming constant physical properties, Navier-Stokes equations (1) can be rearranged to yield

$$\rho \left( \frac{\partial \vec{u}}{\partial t} + (\vec{u} \cdot \nabla) \vec{u} \right) = -\nabla p + \mu \nabla^2 \vec{u} \quad \nabla \cdot \vec{u} = 0 \quad (15)$$

which is the most common form of the Navier-Stokes equations for incompressible single-phase flows.

#### 3.1. Energy conservation

The evolution of kinetic energy,  $E_k = (\vec{u}, \rho \vec{u})$ , in a single-phase flow is obtained by taking the inner product of  $\vec{u}$  and equation (15), which, in the absence of external

forces and without contributions from the boundaries, yields:

$$\frac{dE_k}{dt} = -\rho(\vec{u}, (\vec{u} \cdot \nabla)\vec{u}) - (\vec{u}, \nabla p) + \mu(\vec{u}, \nabla^2 \vec{u}) = -\mu \|\nabla \vec{u}\|^2 \leq 0 \quad (16)$$

Due to the skew-symmetry of the convective operator (i.e.,  $(\vec{u} \cdot \nabla) = -(\vec{u} \cdot \nabla)^*$ ), the contribution of this term to kinetic energy is null. Duality of the gradient operator with divergence (i.e.,  $\nabla^* = -\nabla \cdot$ ) together with the incompressible constrain of the velocity ( $\nabla \cdot \vec{u} = 0$ ) results in a null contribution of the pressure term to kinetic energy [16]. Finally, by exploiting again the duality between gradient and divergence in the viscous term, this results in a negative-definite operator,  $\mu(\vec{u}, \nabla^2 \vec{u}) = -\mu(\nabla \vec{u}, \nabla \vec{u}) = -\mu \|\nabla \vec{u}\|^2$ , which, as expected, dumps kinetic energy.

### 3.2. Symmetry-preserving discretization

We are now going to review the well-know symmetry-preserving, second-order, staggered, finite volume discretization introduced by Verstappen and Veldman in [15], which was subsequently extended to fourth order in [16], from the algebraic perspective by means of the tools introduced in Section 2.1. This lays the foundation of the newly developments introduced in Section 4. The discretization in a staggered grid starts by defining the discrete divergence operator,  $D$ , directly from the Gauss-Ostrogradsky theorem

$$\int_{\Omega} \nabla \cdot \vec{u} dV = \int_{\partial\Omega} \vec{u} \cdot \vec{n} dS \approx -T_{FC} A_F u_f = M_C D u_f, \quad (17)$$

where  $M_C \in \mathbb{R}^{|C| \times |C|}$  stands for the metric of the cells, which is a diagonal matrix containing cells volume.  $T_{FC} \in \mathbb{R}^{|C| \times |F|}$  takes care of the appropriate sum of fluxes over the faces and  $A_F \in \mathbb{R}^{|F| \times |F|}$  is the diagonal matrix containing the surface of all faces. Finally  $u_f$  stands for the staggered velocities. We can rearrange equation (17) to yield

$$D = -M_C^{-1} T_{FC} A_F, \quad (18)$$

this leads to  $D \in \mathbb{R}^{|C| \times |F|}$ , as expected for a staggered grid arrangement. Next, the discrete gradient operator,  $G$ , is constructed to preserve duality

$$(u_f, G p_c)_F = -(D u_f, p_c)_C, \quad (19)$$

where  $(\mathbf{a}_c, \mathbf{b}_c)_C = \mathbf{a}_c^T \mathbf{M}_C \mathbf{b}_c$  stands for the weighted inner product in the cell space,  $C$ . It can be defined conversely for the face space,  $F$ . Further details on inner products can be found in Appendix A.

In the context of Navier-Stokes equations, preserving this duality at the discrete level results into a null contribution of the pressure term to kinetic energy [16]

$$\mathbf{G} = -\mathbf{M}_F^{-1} \mathbf{D}^T \mathbf{M}_C \quad (20)$$

where  $\mathbf{M}_F \in \mathbb{R}^{|F| \times |F|}$  corresponds to the metric of the face space, and thus the definition of such a metric induces the proper construction of  $\mathbf{G}$ . This is nothing but the definition of the staggered control volume. Notice that  $\mathbf{G} \in \mathbb{R}^{|F| \times |C|}$ . Again, this locates gradients at faces, as expected for a staggered discretization.  $\mathbf{M}_F$  is defined as

$$\mathbf{M}_F = \Delta x_F \mathbf{A}_F \quad (21)$$

Note that  $\Delta x_F \in \mathbb{R}^{|F| \times |F|}$  is the diagonal arrangement of the distance between cell centers across the face, while  $\mathbf{A}_F \in \mathbb{R}^{|F| \times |F|}$  is also diagonal and contains face surfaces. The final form of  $\mathbf{G}$  results in

$$\mathbf{G} = (\Delta x_F)^{-1} \mathbf{T}_{CF} \quad (22)$$

where the standard second-order approximation of the gradient arises naturally from the definition of the staggered control volume (i.e., one induces the other).

By concatenation, the discretization of the scalar Laplacian operator,  $L$ , the essential element of the FSM, can be defined as follows

$$\int_{\Omega} \nabla^2 p dV \approx \mathbf{M}_C L \mathbf{p}_c = \mathbf{M}_C \mathbf{D} \mathbf{G} \mathbf{p}_c \quad (23)$$

As expected,  $L \in \mathbb{R}^{|C| \times |C|}$ . We can expand the final integrated form of the discrete Laplacian as

$$\mathbf{M}_C L = -\mathbf{T}_{FC} \mathbf{A}_F (\Delta x_F)^{-1} \mathbf{T}_{CF} \quad (24)$$

where such a discretization results in a negative-definite operator since  $\mathbf{A}_F$  and  $\Delta x_F$  are positive-definite, and  $\mathbf{T}_{FC} = \mathbf{T}_{CF}^T$ . This is the ultimate responsible of the diffusive character of viscosity in the context of Navier-Stokes equations.

Finally, the convective term can proceed as in Hicken et al. [37] in order to construct a skew-symmetric discretization. Even when dedicated convective operators may

be constructed for Cartesian meshes, this provides with a more flexible approach. The idea is to construct proper face-to-cell and cell-to-face shift operators in order to exploit the collocated convective operator as

$$\mathbf{C}(\mathbf{u}_f)_F = \Gamma_{f \rightarrow c} (\mathbf{I}_d \otimes \mathbf{C}(\mathbf{u}_f)_C) \Gamma_{c \rightarrow f} \quad (25)$$

which guarantees skew-symmetry as far as the vector-valued shift operators are transpose (i.e.,  $\Gamma_{f \rightarrow c} = \Gamma_{c \rightarrow f}^\top$ ), as it is the case. Further details can be found in [15, 16, 37, 38] and references therein.

### 3.3. Analysis

By preserving (skew-)symmetries of the operators, as it was described above, the conservation of kinetic energy is guaranteed in the semi-discrete setup (i.e., up to temporal integration [39]), mimicking then the continuous behavior of the system. In particular, the semi-discretized energy balance equation reads

$$\frac{dE_k}{dt} = -(\mathbf{u}_f, \mathbf{C}(\mathbf{u}_f)_F \mathbf{u}_f)_F - (\mathbf{u}_f, \mathbf{G} \mathbf{p}_c)_F + \mu (\mathbf{u}_f, \mathbf{L}_F \mathbf{u}_f)_F \leq 0, \quad (26)$$

which is the discrete counterpart of equation (16). As expected, the only term contributing to kinetic energy is the viscous one, i.e.,  $\mu (\mathbf{u}_f, \mathbf{L}_F \mathbf{u}_f)_F$ , where  $\mathbf{L}_F$  is the standard, negative-definite, staggered diffusive operator [16]. Note that this holds thanks to the specific construction of the operators involved and if the incompressibility constraint of velocity is satisfied at the discrete level as well (i.e.,  $\mathbf{D} \mathbf{u}_f = \mathbf{0}_c$ ).

## 4. Energy-preserving discretization of multiphase flows

Multiphase flows present discontinuities at the interface due to the difference of physical properties and the existence of interfacial phenomena, namely, surface tension. This section develops, on top of the symmetry-preserving scheme reviewed in the previous section, a novel energy-preserving scheme for the discretization of curvature. Curvature plays a key role in the development of discontinuities,  $[\cdot]$ , across the interface as

$$[\sigma] \hat{\eta}_i = -\gamma \kappa \hat{\eta}_i \quad (27)$$

where  $\gamma$  states for the surface tension coefficient, which we assume constant. This configures the resulting surface tension force, which acts at the interface by imposing a jump condition into the stress tensor which “pulls” the interface towards a lower free energy state. The original governing equations (1) can then be reformulated as

$$\rho \left( \frac{\partial \vec{u}}{\partial t} + (\vec{u} \cdot \nabla) \vec{u} \right) = -\nabla p + \nabla \cdot \tau \quad \nabla \cdot \vec{u} = 0 \quad (28)$$

$$[p] = \hat{\eta}_i^T [\tau] \hat{\eta}_i - \gamma \kappa \quad (29)$$

where  $\sigma = -p\mathbb{1} + \tau$  is split into hydrostatic and deviatoric. The discussion about the discretization of  $\tau$  is out of the scope of this work, so the interested reader is referred to Lalanne et al. [26] for a thoughtful discussion on this topic. At this point, it is assumed that  $\tau$  presents a prescribed discontinuity at the interface.

#### 4.1. Energy conservation

Regardless of viscous dissipation, incompressible, multiphase flows, do not preserve kinetic energy. Instead, surface ( $E_p = \gamma A$ ) and kinetic ( $E_k = (\vec{u}, \rho \vec{u})$ ) energy are exchanged through the pressure term [28] such that, except for the aforementioned viscous term, mechanical energy is conserved. Interface deformation results then in a transfer, through the pressure jump, between surface and kinetic energy. In order to analyze such a transfer, we start by analyzing the evolution of kinetic energy for multiphase flows, which is obtained by taking the inner product of  $\vec{u}$  and, this time, the general formulation of an incompressible, Newtonian fluid given in equation (28)

$$\frac{dE_k}{dt} = -(\vec{u}, (\rho \vec{u} \cdot \nabla) \vec{u}) - (\vec{u}, \nabla p) + (\vec{u}, \nabla \cdot \tau) \quad (30)$$

As stated in Section 3.1, the skew-symmetry of the convective term results in a null contribution to kinetic energy, while the stress term includes an extra contribution due to the discontinuity at the interface stated in equation (27).

$$-(\vec{u}, \nabla p) + (\vec{u}, \nabla \cdot \tau) = (\nabla \cdot \vec{u}, p) - (\nabla \vec{u}, \tau) - \int_{\Gamma} [p] \vec{u} \cdot \hat{\eta}_i dS + \int_{\Gamma} [\tau] \vec{u} \cdot \hat{\eta}_i dS \quad (31)$$

Further details on the treatment of discontinuities within the inner product can be found in Appendix A.

Next, by considering an incompressible flow ( $\nabla \cdot \vec{u} = 0$ ), taking the pressure jump as stated in equation (29) and splitting  $\nabla \vec{u}$  into symmetric ( $S$ ) and skew-symmetric ( $W$ ) parts we obtain

$$\begin{aligned}
\frac{dE_k}{dt} &= -(\vec{u}, \nabla p) + (\vec{u}, \nabla \cdot \tau) = -(\nabla \vec{u}, \tau) - \int_{\Gamma} \vec{u} [p] \hat{\eta}_i dA + \int_{\Gamma} \vec{u} [\tau] \hat{\eta}_i dA \\
&= -(\nabla \vec{u}, \tau) + \gamma \int_{\Gamma} \kappa \vec{u} \cdot \hat{\eta}_i dA \\
&= -(S + W, 2\mu S) + \gamma \int_{\Gamma} \kappa \vec{u} \cdot \hat{\eta}_i dA \quad (32) \\
&= -2(S, \mu S) + \gamma \int_{\Gamma} \kappa \vec{u} \cdot \hat{\eta}_i dA \\
&= -2 \|\sqrt{\mu} S\|^2 + \gamma \int_{\Gamma} \kappa \vec{u} \cdot \hat{\eta}_i dA \quad \square
\end{aligned}$$

As expected, viscosity results in a negative contribution to kinetic energy, whereas surface tension can take any sign depending on whether the interface is expanding or contracting.

On the other hand, the evolution of surface energy is related to the evolution of the interfacial area. By considering Helmholtz's free energy [40]

$$dF = \gamma dA, \quad (33)$$

and plugging it in equation (9), we state that

$$\frac{dE_p}{dt} = \int_{\Gamma} \frac{d}{dt} dF = \gamma \int_{\Gamma} \frac{d}{dt} dA = -\gamma \int_{\Gamma} \kappa \vec{u} \cdot \hat{\eta}_i dA \quad (34)$$

Finally, performing a global balance of energy by combining equations (32) and (34), we obtain

$$\frac{dE_m}{dt} = \frac{dE_k}{dt} + \frac{dE_p}{dt} = -2 \|\sqrt{\mu} S\|^2 \quad (35)$$

As expected, surface tension does not play a role in the dissipation of energy, but rather produce a dynamic exchange between kinetic and surface ones of magnitude  $\gamma \int_{\Gamma} \kappa \vec{u} \cdot \hat{\eta}_i dA$ .

#### 4.2. Energy-preserving discretization

In the same spirit that symmetry-preserving methods aim at ensuring a null contribution of both pressure and convective terms in equation (16) at the discrete level, the

task in a multiphase flow simulation adds to the requirements to preserve the proper transfer between kinetic and potential energies as

$$\frac{dE_m}{dt} = \frac{dE_k}{dt} + \frac{dE_p}{dt} \quad (36)$$

Namely, if symmetry-preserving schemes were constructed to satisfy at a discrete level equation (19), energy-preserving methods also satisfy the discrete version of equation (9) in order to properly capture energetic exchanges between kinetic and surface energies. This requires the reformulation of the convective term for variable density flows to preserve skew-symmetry, as proposed by Rozema et al. [41], which however is out of the scope of this work. Nonetheless, the transfer between kinetic and surface energy occurs through the surface tension term as

$$\frac{d}{dt} (\mathbf{G}\theta_c, \hat{\mathbf{n}}_f)_F = -(\mathbf{U}\mathbf{G}\theta_c, \mathbf{k}_f)_F \quad (37)$$

where  $\mathbf{U} = \text{diag}(\mathbf{u}_f) \in \mathbb{R}^{|F| \times |F|}$  is the diagonal arrangement of face velocities,  $\theta_c \in \mathbb{R}^{|C|}$  is the cell-centered marker function vector and  $\mathbf{k}_f \in \mathbb{R}^{|F|}$  is the staggered curvature vector. We consider the advection of the marker function in terms of the discretized equation (5)

$$\frac{d\theta_c}{dt} = -\mathbf{C}(\mathbf{u}_f)_C \theta_c \quad (38)$$

where  $\mathbf{C}(\mathbf{u}_f)_C \in \mathbb{R}^{|C| \times |C|}$  stands for the convective term of the marker function. It may usually include a high-resolution scheme, as we shall see later, but so far we consider it as a single operator. We disregard the role of recompression stages in time derivatives but rather consider them as correction steps, which is discussed later on this section. As previously exposed for the continuum case, we can proceed by constructing the discrete counterpart of equation (14) as

$$\left( \mathbf{G} \frac{d\theta_c}{dt}, \hat{\mathbf{n}}_f \right)_F = -(\mathbf{U}\mathbf{G}\theta_c, \Upsilon \mathbf{D}\hat{\mathbf{n}}_f)_F \quad (39)$$

where a new shift operator,  $\Upsilon \in \mathbb{R}^{|F| \times |C|}$ , is introduced in order to map the curvature from cells to faces. Exploiting the duality of the discrete gradient and divergence operators, equation (19), we obtain

$$-\left( \frac{d\theta_c}{dt}, \mathbf{D}\hat{\mathbf{n}}_f \right)_C = -(\mathbf{U}\mathbf{G}\theta_c, \Upsilon \mathbf{D}\hat{\mathbf{n}}_f)_F \quad (40)$$

By subsequently expanding the inner products, we obtain

$$-\left(\frac{d\theta_c}{dt}\right)^T M_C D\hat{n}_f = -UG\theta_c^T M_F \Upsilon D\hat{n}_f \quad \forall \hat{n}_f \quad (41)$$

which must hold regardless of the interface normal,  $\hat{n}_f$ , and consequently independently of the cell-centered curvature,  $D\hat{n}_f$ . This implies that

$$-\left(\frac{d\theta_c}{dt}\right)^T M_C = -(UG\theta_c)^T M_F \Upsilon \quad (42)$$

must hold at any time, while releasing a degree of freedom regarding the definition of the normal. We can now plug equation (38) in for the time derivative and expand the transpose terms

$$-\left(\frac{d\theta_c}{dt}\right)^T M_C = (C(u_f)_C \theta_c)^T M_C = \theta_c^T C(u_f)_C^T M_C = -\theta_c^T G^T U^T M_F \Upsilon \quad \forall \theta_c \quad (43)$$

which should hold for any  $\theta_c$ . This leads to

$$C(u_f)_C^T M_C = -G^T U^T M_F \Upsilon \quad (44)$$

where, exploiting the diagonal arrangement of both  $U$  and  $M_F$  to cast  $G^T U^T M_F$  into  $G^T M_F U$ , we can use equation (20) to obtain the final condition as

$$-(M_C C(u_f)_C)^T = M_C D U \Upsilon \quad (45)$$

From where we can infer that the convective scheme of the marker function determines the curvature shift operator. This identity guarantees that energy transfers are balanced and thus total mechanical energy,  $E_m$ , is preserved up to temporal integration, in the same way that kinetic energy,  $E_k$ , is preserved in the symmetry-preserving discretization presented in Section 3.2 for the single-phase case.

Regarding the construction of  $C(u_f)_C$ , any high-resolution scheme can be embedded into the algebraic form  $C(u_f)_C = DU\Psi$ , where  $\Psi \in \mathbb{R}^{|F| \times |C|}$  is the actual high-resolution cell-to-face interpolator. For the CLS, this typically corresponds with SUPERBEE [11]. We can split  $\Psi$  as  $\Psi = \Pi + \Lambda$  [42], to produce

$$C(u_f)_C = DU(\Pi + \Lambda) \quad (46)$$



This represents the symmetric (DUII) and skew-symmetric (DUA) components of  $C(u_f)_C$ . The extension to VOF schemes, nicely summarized by Patel et al. [43], requires a previous casting of the advection scheme into the same framework introduced in [42]. Plugging equation (46) into equation (45) results in the final form of the dedicated cell-to-face interpolation for curvature

$$\Upsilon = \Pi - \Lambda \quad (47)$$

which guarantees a proper potential and kinetic energy transfer. An illustrative example can be seen in Figure 3. In short, any upwind-like component used for the advection of  $\theta_c$  turns into a downwind-like component for the interpolation of  $k_f$ . This can be compared with the second-order midpoint rule used by Olsson and Kreiss where  $\Upsilon = \Pi$  [11].

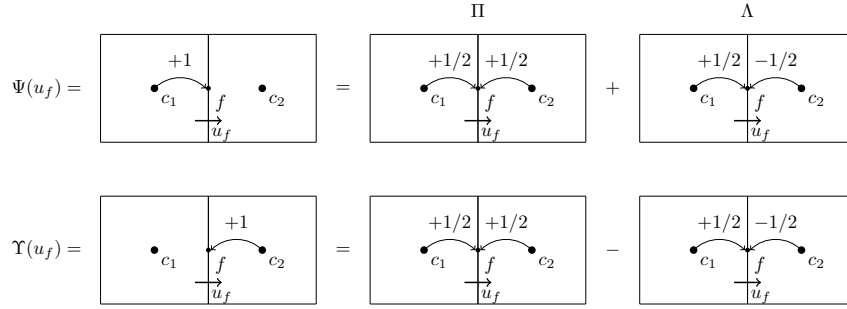


Figure 3: Example of a particular high-resolution scheme  $\Psi$  for the advection of  $\theta_c$  (in this example, the well-known upwind scheme) and the corresponding dedicated curvature interpolator,  $\Upsilon$ . In this case, the interpolation scheme for curvature is downwind.

### 4.3. Analysis

By mimicking equations (30) and (32) we obtain the discrete counterpart of kinetic energy as

$$\frac{dE_k}{dt} = \gamma (UG\theta_c, \Upsilon k_c) + \mu (u_f, L_F u_f), \quad (48)$$

which assumes a proper discretization of all other terms described in Section 3. We proceed similarly for potential energy by mimicking equation (34) to define discrete

potential energy as

$$\frac{dE_p}{dt} = \gamma \left( \mathbf{G} \frac{d\theta_c}{dt}, \hat{n}_f \right) \quad (49)$$

We obtain the semi-discretized total energy equation by combining equations (48) and (49), which, in combination with equation (39) yields

$$\frac{dE_m}{dt} = \frac{dE_k}{dt} + \frac{dE_p}{dt} = \gamma (\mathbf{U}\mathbf{G}\theta_c, \Upsilon\mathbf{k}_c) + \mu (\mathbf{u}_f, \mathbf{L}_F\mathbf{u}_f) + \gamma \left( \mathbf{G} \frac{d\theta_c}{dt}, \hat{n}_f \right) = \mu (\mathbf{u}_f, \mathbf{L}_F\mathbf{u}_f) \leq 0 \quad (50)$$

Which can be compared with equation (35) to check that (in the absence of viscosity) the proposed numerical setup satisfies energy conservation up to temporal integration. Note that, as in the single-phase flow, this holds for any incompressible flow at the discrete level as well (i.e.,  $\mathbf{D}\mathbf{u}_f = 0_c$ ).

The role of interface recompression deserves a special remark. Customarily included in the level set literature [32, 11], its role is to recover the interface sharpness that may have been deteriorated by the convective schemes by taking additional, correcting steps after an initial advection stage. Nonetheless, even when performed conserving mass, as in [11, 12], the nature of recompression results in a non-null contribution to potential energy, which violates the conservation of mechanical energy. For this reason, the energy-preserving method presented here disregards recompression to focus on the physical coupling between marker advection and momentum transport. Similarly, other interface capturing schemes may consider additional steps aimed at recovering interface quality and/or mass conservation [44]. While the results presented here allow to adopt this formulation into the momentum equation, including additional correcting steps require an individualized analysis.

## 5. Results

Equipped with the discretization described in Section 4, we assess its performance for canonical tests for multiphase flow systems. We focus on inviscid simulations in order to isolate the performance of our newly developed discretization. Equations (1)

and (5) are discretized according to the above-mentioned discretization. These read as

$$\frac{du_f}{dt} = -C(u_f)_F u_f - G p_c + \gamma K_F G \theta_c \quad (51)$$

$$\frac{d\theta_c}{dt} = -C(u_f)_C \theta_c \quad (52)$$

where  $K_F = \text{diag}(\Upsilon k_c)$  is the diagonal arrangement of the staggered curvature.

Density ratio has been fixed to 1 in order to isolate the surface tension term, simplify the discretization of the convective term and facilitate the solution of the pressure-velocity decoupling. Nonetheless, as far as the convective term preserves skew-symmetry and the Poisson equation is solved exactly, ratios different than 1 may be included flawlessly. Surface tension forces are included as mentioned in Section 4

The system is integrated in time with a second-order Adams-Bashforth scheme while the pressure-velocity decoupling is achieved with a classical FSM [14]. An efficient FFT decomposition in the periodic direction coupled with a Cholesky solver is used to ensure divergence-free velocity fields to machine accuracy.

All simulations are carried on a  $\Omega = [2H \times 2H]$  square domain, where  $H$  is both the semi-width and semi-height of the cavity. Top and bottom faces present periodic boundary conditions, while at the sides no-flux boundary conditions is imposed for the marker function (i.e.,  $\nabla \theta \cdot \hat{n}_{wall} = 0$ ) while free slip is set for velocity (i.e.,  $\vec{u} \cdot \hat{n}_{wall} = 0$ ). This enforces conservation of all physical quantities.

Linear perturbation theory is used to obtain reference values for time, velocity and pressure. Note that linear perturbation assumes small interfacial deformation, while the cases presented here do not necessarily satisfy such a condition, it still provides with a reference value. Energy levels are scaled by and referenced to the initial observed mechanical energy. Because all simulations start with a fluid at rest and an elongated interface, kinetic energy evolves in the positive region (i.e., velocity is higher than or equal to the initial one) while potential energy evolves in the negative region (i.e., elongation is less than or equal to the initial one).

Tests are carried in order to compare the standard midpoint rule used for the interpolation of curvature proposed by Olsson and Kreiss [11] with the newly developed interpolation scheme. Recompression has been initially set aside in order to evaluate

its impact on both schemes in a subsequent analysis. It is computed as

$$\frac{d\theta_c}{d\tau} + D\Gamma_{f \rightarrow c} N_C (I_C - \Theta_C) \theta_c = DE_F G \theta_c, \quad (53)$$

where  $\tau$  stands for pseudo-time,  $\Gamma_{f \rightarrow c}$  is vector-valued shift operator,  $N_C \in \mathbb{R}^{d_C \times |C|}$  maps scalars to vector fields aligned with the interface normal, while  $\Theta_C = \text{diag}(\theta_c)$  and  $E_F = \text{diag}(\epsilon_i)$  are the diagonal arrangements of, respectively,  $\theta_c$  and  $\epsilon$ ; where  $\epsilon$  is the face-centered smoothing factor defined in Section 2.2.1. Further details can be found in Olsson and Kreiss [11] for the CLS and in Trias et al. [38] for the construction of the operators.

### 5.1. Cylindrical column

The classical setup of a zero gravity cylindrical column of liquid is tested in order to show the impact of the newly proposed method into spurious currents. The section of the column is located at the center of the domain and is given a radius of  $R_0 = 0.3H$ . Velocity is initially stagnant and that is how it should remain throughout the simulation; however, spurious currents are expected to appear due to errors in the calculation of curvature [27]. The initial setup is depicted in Figure 4.

Linear perturbation theory provides with the time period for an initially cylindrical interface perturbed as  $r(\theta) = R_0 + r_p \cos(s\theta)$ , where  $s = 2, 3, 4, \dots$  corresponding to ellipsoidal, triangular or rectangular deformations, respectively [45]. Because linear theory predicts perfect equilibrium for both  $s = 0$  and  $s = 1$ , we arbitrarily assume an ellipsoidal perturbation (i.e.,  $s = 2$ ) in order to obtain a reference state. The oscillation period can be computed for any  $s$  as  $T = 2\pi / \sqrt{2\rho R_0^3 / \gamma s(s^2 - 1)}$  [46], while the characteristic length scale is  $L = 2\pi R_0$ , which leads a characteristic speed of  $c = L/T = \sqrt{\gamma s(s^2 - 1) / 2\rho R_0^3}$ , while pressure is referenced to  $\rho c^2$ . Integration is carried over  $5T$ .

Results in Figure 5 show how the newly proposed method (right column) results in an energy stable simulation by counterbalancing the numerical increase in kinetic energy with a decrease of potential energy. This yields to a stagnant situation in which both kinetic and potential energy restore their initial values (i.e.,  $E_k = 0$  and  $E_p = 0$ ).

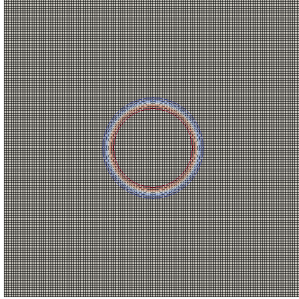


Figure 4: Initial setup of the marker function for cylindrical column test case in a  $128 \times 128$  mesh. Contour lines are plotted for  $\Delta\theta = 0.1$ .

On the other hand, the standard midpoint rule interpolation for curvature (left column) results in an increase in total energy .

In Figure 6 it can be seen how the newly developed curvature interpolation scheme (right) provides, first of all, an order of magnitude smaller oscillations that the standard one produces (left). In addition, there is a dramatic increase in the flow quality within the interface, extending the benefits of the high resolution advection scheme for the marker into the velocity field. On the other hand, the use of the standard midpoint rule for updating curvature pollutes the flow within both phases.

It is remarkable how, despite initializing the interface to a theoretical minimum energy situation (i.e., cylindrical cross-section), numerical imbalances when computing curvature does not reflect such a situation [27]. Nonetheless, the use of an energy-preserving scheme acts in order to keep energy constant, and so counter-balances such an artificial movement by modifying the curvature accordingly. This results in a robust method which eventually is perturbation-proof.

In comparison with Figure 5, Figure 7 shows the impact of recompression in both schemes. As can be seen, the newly developed interpolation method can do little in terms of energy, as the recompression stage increases the energy of the system. Actually, we see how the increase in kinetic energy is even higher than in the previous case, with no recompression associated.

On the other hand, Figure 8 shows how the velocity field is clearly distorted in

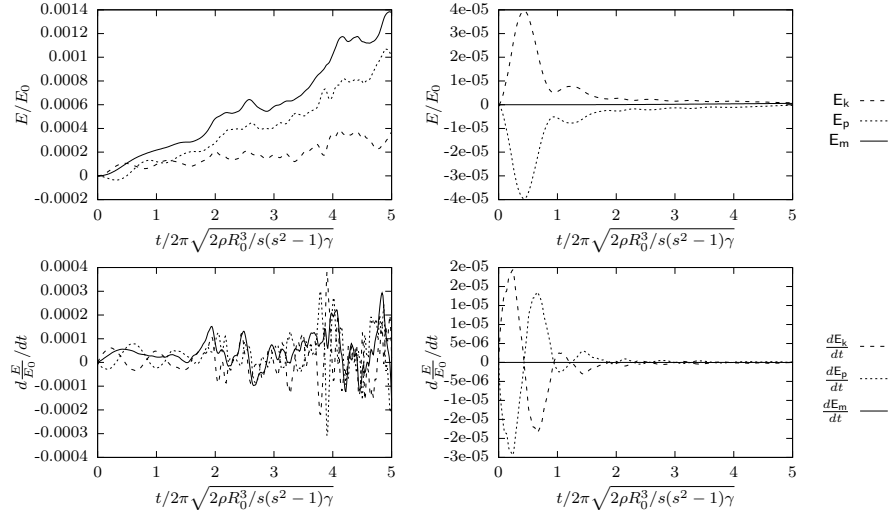


Figure 5: Energy evolution of the cylindrical section for a pure advection case (i.e., no recompression) with the standard interpolation of Olsson and Kreiss [11] for the curvature (left) and the newly proposed method (right) in a  $128 \times 128$  mesh. Top rows show the discrete values of kinetic ( $E_k$ ), potential ( $E_p$ ) and total ( $E_m$ ) energy. Bottom rows show their semi-discretized time derivative according to equations (48), (49) and (50), respectively.

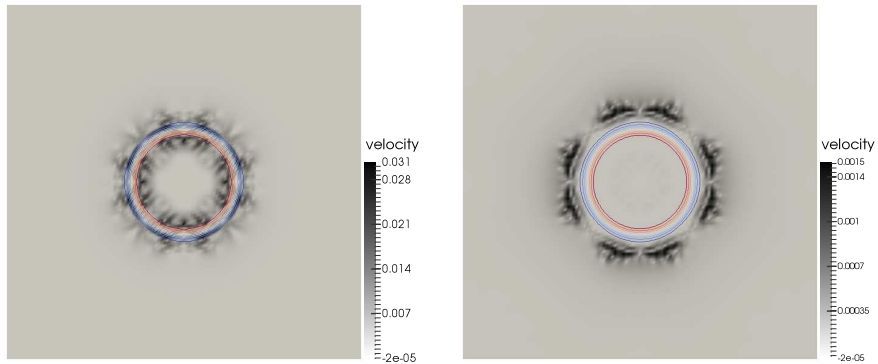


Figure 6: Velocity magnitude and interface location at  $t = 5T$  for a cylindrical column in a  $128 \times 128$  mesh advected without recompression. Left figure uses the standard midpoint rule while the right one uses the newly developed energy-preserving one. Contour lines are plotted for  $\Delta\theta = 0.1$ .

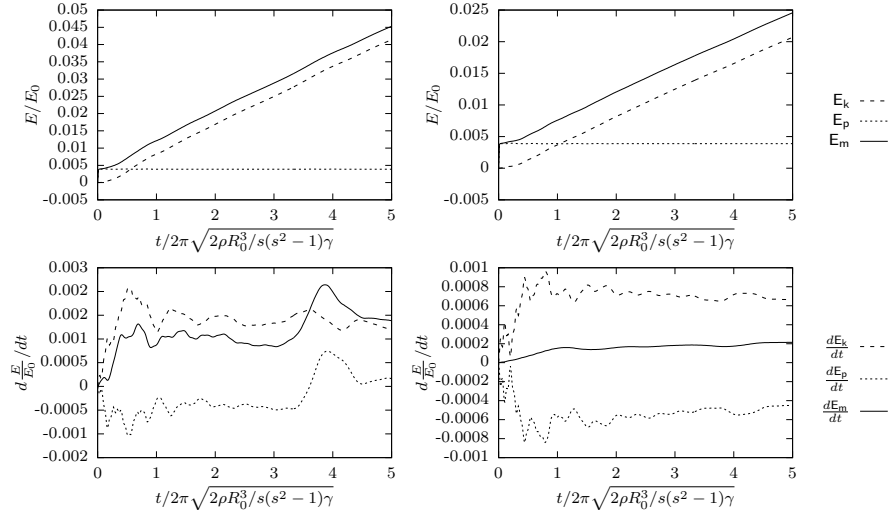


Figure 7: Energy evolution of cylindrical column with the complete Olsson and Kreiss method [11] with a single recompression stage (left), and the same method including the modified curvature interpolation (right) in a  $128 \times 128$  mesh. Top rows show the discrete values of kinetic ( $E_k$ ), potential ( $E_p$ ) and total ( $E_m$ ) energy. Bottom rows show their semi-discretized time derivative according to equations (48), (49) and (50), respectively.

both cases, degrading the solution with respect to the pure advection algorithm one and two orders of magnitude with respect to the midpoint and the energy-preserving interpolation schemes, respectively. Noticeably, we still retain, even by including the recompression scheme, a higher quality of the velocity field within the bounded region for the newly developed interpolation scheme. The impact of recompression in the overall quality of the solution is discussed in Section 6.

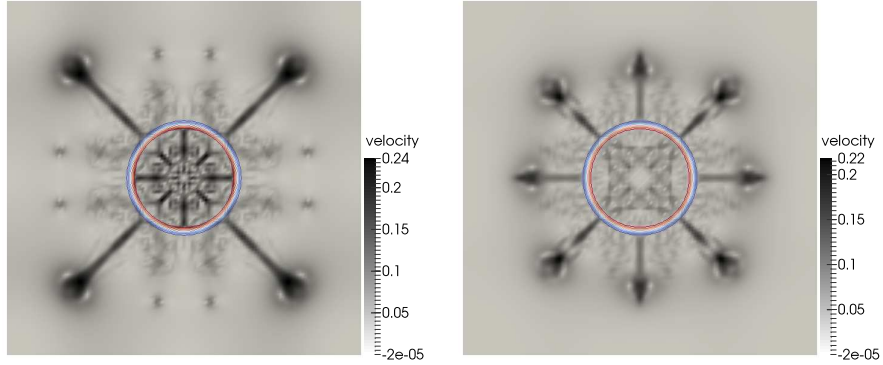


Figure 8: Velocity magnitude and interface location at  $t = 5T$  for a cylindrical column in a  $128 \times 128$  mesh advected with a single recompression step. Left figure uses the standard 2nd order shift operator while the right one uses the newly developed energy-preserving one. Contour lines are plotted for  $\Delta\theta = 0.1$ .

### 5.2. Oscillating ellipsoidal column

In order to stretch the previous result to a dynamic equilibrium situation, an ellipsoidal section is set by distorting the initially cylindrical case. As in the cylindrical water column, spurious currents may appear, while this time they accompany legitimate currents as a result of regions with a moderate non-constant curvature. The ellipse is centered in the domain and is defined by  $x = 0.5\cos(\alpha)$  and  $y = 0.3\sin(\alpha)$ , where  $\alpha \in [0, 2\pi)$ . Velocity field is initialized at rest and should follow to the oscillation of the ellipsoid throughout the simulation. The initial setup is depicted in Figure 9.

In the same fashion that in the cylindrical water column described above, linear perturbation theory is employed in order to obtain a reference state. Characteristic length is set to  $L = 2\pi R_0$ , where  $R_0 = 0.3$ . Time, velocity and pressure scales used are the same than those for the cylindrical section case.

Figure 10 shows how, while the standard midpoint interpolation (left) clearly increases the mechanical energy of the system, the newly proposed energy-preserving interpolation scheme for curvature (right) preserves mechanical energy, which yields physically consistent results and numerically stable simulations. There is, however, both positive and negative offsets for kinetic and potential energies. While kinetic and



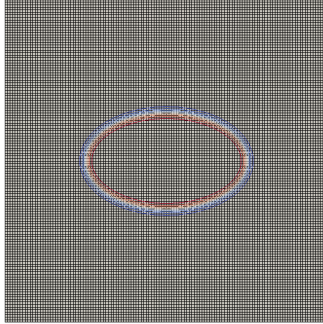


Figure 9: Initial setup of the marker function for the oscillating ellipse test case in a  $128 \times 128$  mesh. Contour lines are plotted for  $\Delta\theta = 0.1$ .

potential energy are supposed to oscillate between 0 and its maximum or minimum for an ideal harmonic oscillator, we observe that this is not the case. This is explained by an imbalance in the momentum equation, which provides an artificial acceleration in the fluid, resulting in an increase of the kinetic energy base state [47]. By virtue of the energy-preserving scheme the oscillation gap for potential energy is reduced accordingly, resulting in a decrease of the elongation amplitude. This plays a relevant role in the next case presented, the capillary wave, which is further discussed in the next subsection. Despite this well-known issue results still show the expected oscillatory behavior of the ellipsoid. This can be checked from the bottom row of Figure 10, where the magnitude of the energy transfers remains approximately constant throughout the simulation. In terms of the oscillating behavior, the increase in mechanical energy for the naive interpolation results not only in artificially higher values of kinetic energy, but also in a phase difference with respect to the energy-preserving one.

Figure 11 presents the marker and velocity fields after  $t = 5T$  with a pure advection scheme. Results for the energy-preserving scheme (right) show a shift in phase with respect to the midpoint interpolation scheme (left). Velocity is not only higher for the naive approach, but also the shape of the interface provides with non-physical curvature, as it can be observed by the kink appearing along the horizontal centerline of the ellipsoid (left), which can be compared with the smoother profile present in the energy-preserving approach (right).

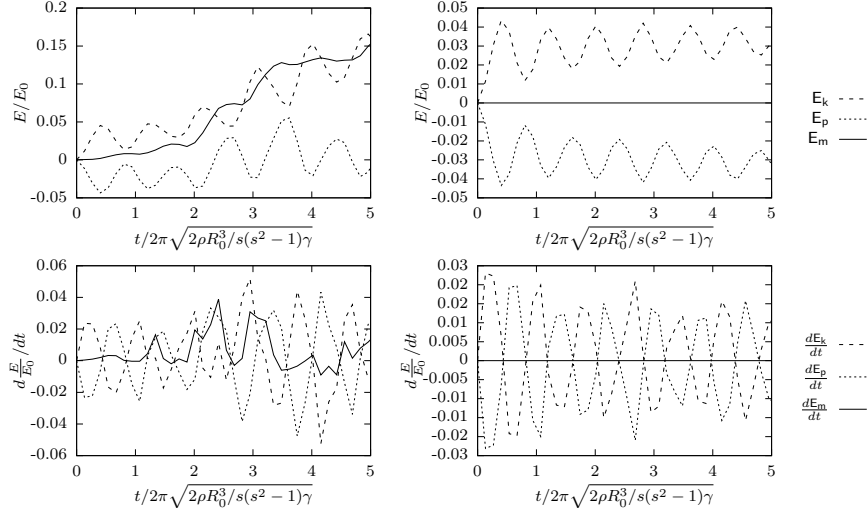


Figure 10: Energy evolution of the ellipsoidal section for a pure advection case (i.e., no recompression) with the standard interpolation of Olsson and Kreiss [11] for the curvature (left) and the newly proposed method (right) in a  $128 \times 128$  mesh. Top rows show the discrete values of kinetic ( $E_k$ ), potential ( $E_p$ ) and total ( $E_m$ ) energy. Bottom rows show their semi-discretized time derivative according to equations (48), (49) and (50), respectively.

In summary, the use of the energy-preserving scheme provides a higher degree of reliability, by preserving mechanical energy also in a dynamical equilibrium situation. Despite the numerical errors in which the discretization of momentum may occur, the method is robust and still preserves mechanical energy.

The results obtained by including a single recompression step into the algorithm are presented in Figure 12. They show how, irrespective of the use of an energy-preserving scheme into the advection scheme, the amount of energy included into the system in order to keep a sharper profile results in a small, but non-physical, increase of mechanical energy. Compared with Figure 10, it can be seen how the difference is not as much in mechanical energy but rather in the nature of the oscillations. While results without recompression still preserve to some extent the oscillating nature of the physical system, recompression produces an enhanced smoothing, resulting in a flat profile in terms of both kinetic and potential energy.

The claim stated above can be clearly seen in Figure 13, where the initial ellipsoid,

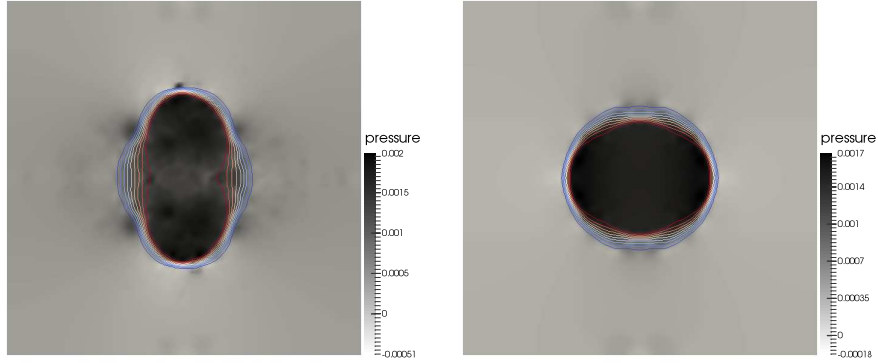


Figure 11: Pressure field and interface location at  $t = 5T$  for the oscillating ellipse in a  $128 \times 128$  mesh advected without recompression. Left figure uses the standard 2nd order shift operator while the right one uses the newly developed energy-preserving one. Contour lines are plotted for  $\Delta\theta = 0.1$ .

expected to present a dynamical equilibrium, results in a fully rounded shape. Besides, Figure 13 shows how the resulting fields, in both cases, are irrespective of the interpolation scheme for curvature used for the advection scheme. Further discussion on the impact of recompression in the final result is discussed in Section 6.

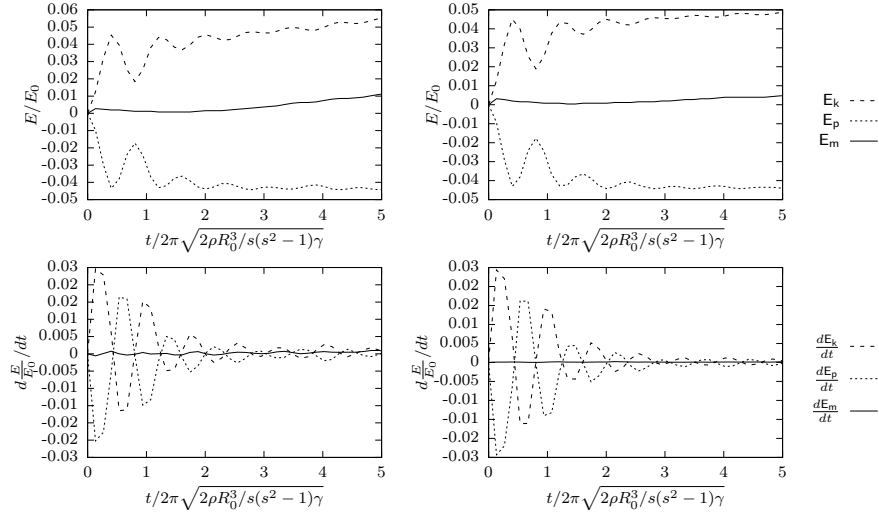


Figure 12: Energy evolution of the oscillating ellipse with the complete Olsson and Kreiss method [11] with a single recompression stage (left), and the same method including the modified curvature interpolation (right) in a  $128 \times 128$  mesh. Top rows show the discrete values of kinetic ( $E_k$ ), potential ( $E_p$ ) and total ( $E_m$ ) energy. Bottom rows show their semi-discretized time derivative according to equations (48), (49) and (50), respectively.

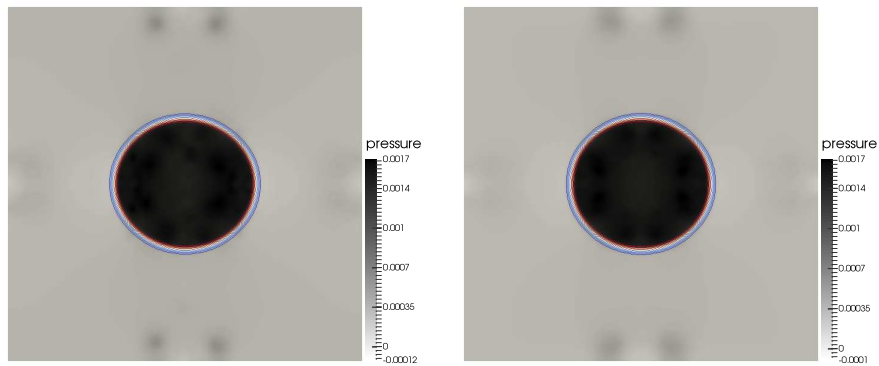


Figure 13: Pressure field and interface location at  $t = 5T$  for the oscillating ellipse in a  $128 \times 128$  mesh advected with a single recompression step. Left figure uses the standard 2nd order shift operator while the right one uses the newly developed energy-preserving one. Contour lines are plotted for  $\Delta\theta = 0.1$ .

### 5.3. Capillary wave

A pure capillary wave is set by originally locating the interface at  $x = 0.2\sin(ky)$ , producing an initial wave along the vertical center line of wavelength  $2\pi/k$ . We set  $k = \pi/H$ , so that a single oscillating period is contained within the domain. Velocity is initially at rest. With the mentioned boundary and initial conditions, the wave is expected to oscillate indefinitely, alternating states of maximum potential energy (i.e., maximum elongation) and minimum kinetic energy (i.e., fluid at rest) and vice-versa. Initial setup is presented in Figure 14.

As is well known from linear perturbation theory [45], the oscillation of the given setup present a characteristic period of  $T = 2\pi \sqrt{2\rho/\gamma k^3 \tanh(kH)}$ , which is used as the reference value for time. On the other hand, the characteristic length scale is  $L = 2\pi/k$ , the wavelength of the perturbation. This yields a characteristic velocity of  $c = L/T = \sqrt{\gamma k \tanh(kH)/2\rho}$ , while pressure is referenced to  $\rho c^2$ , where  $\rho$  stands for the average. Integration in time is set to  $2T$ .

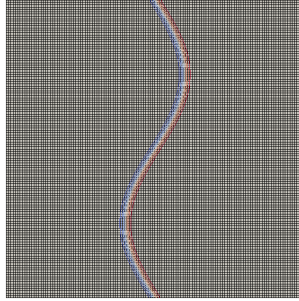


Figure 14: Initial setup of the marker function in a  $128 \times 128$  mesh. Contour lines are plotted for  $\Delta\theta = 0.1$ .

Results in Figure 15 show how the energy preserving discretization proposed in the present work preserves mechanical energy (top row, solid line) by balancing the resulting energy transfers (bottom row, solid line). While the standard midpoint interpolation of curvature results in a non-physical increase of mechanical energy, which ultimately leads to instabilities, the novel proposed method provides a stable discretization.

Even when mechanical energy is conserved in the newly proposed method, both

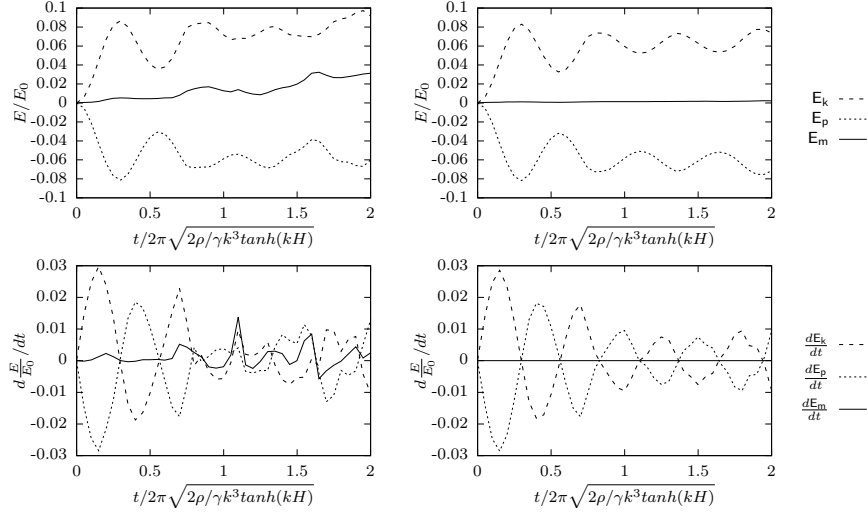


Figure 15: Energy evolution of the capillary wave for a pure advection case (i.e., no recompression) with the standard interpolation of Olsson and Kreiss [11] for the curvature (left) and the newly proposed method (right) in a  $128 \times 128$  mesh. Top rows show the discrete values of kinetic ( $E_k$ ), potential ( $E_p$ ) and total ( $E_m$ ) energy. Bottom rows show their semi-discretized time derivative according to equations (48), (49) and (50), respectively.

the amplitude of kinetic and potential oscillations (Figure 15, top row, right) and the magnitude of the energy transfers (Figure 15, bottom row, right) exhibit a significant damping. The reason behind such a damping is the non-null contribution of surface tension to the momentum equation (the desired result for a closed surface) which produces an artificial acceleration of the fluid. The origin of such artificial acceleration lies in the discretization of curvature, particularly the computation of normals, which is at the origin of the errors that propagate to the momentum equation. This non-physical increase in kinetic energy manifests itself as an increase of the base level of kinetic energy at off-peaks, as can be seen in the top row of Figure 15. While naive interpolation techniques are unresponsive to such energy increments, the new energy-preserving method adjusts the transfers between kinetic and potential energies through surface tension to keep mechanical energy constant. As a result, the artificial and progressive increase in the kinetic energy level leaves no room to capillary oscillations, driving the system to a stagnant, but stable, situation.

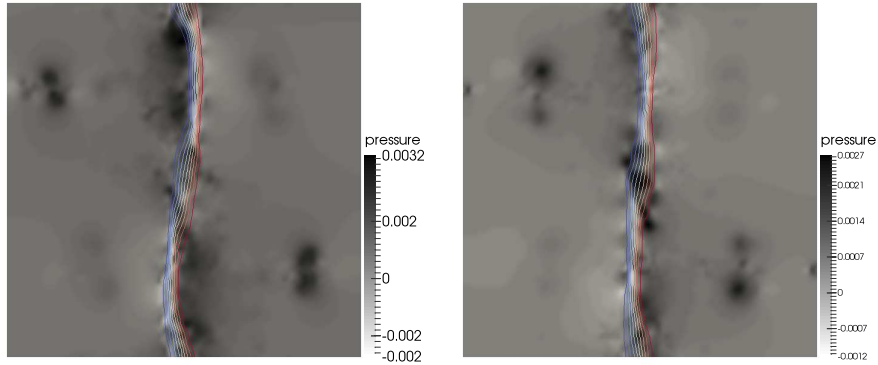


Figure 16: Pressure field and interface location at  $t = 2T$  for a pure capillary wave in a  $128 \times 128$  mesh advected without recompression. Left figure uses the standard 2nd order shift operator while the right one uses the newly developed energy-preserving one. Contour lines are plotted for  $\Delta\theta = 0.1$ .

Figure 17, on the other hand, includes a recompression step into the evolution of the wave. Results show clearly how, despite its known advantages [11], the resulting solution does not preserve energetic balances but rather increase total energy of the system, leading to eventual instabilities. It can be seen how the gain in sharpness introduced by recompression schemes is at the expenses of destroying the advantages of the energy-preserving discretization. Results in Figure 18 can be compared with those of Figure 16, which shows how recompression increases the total energy of the system. Namely, the scale in Figure 18 shows how velocity magnitudes are clearly higher regardless of the advective step is energy-preserving or not. Among them, the energy-preserving scheme shows milder velocity fields. This role of recompression is analyzed in Section 6.

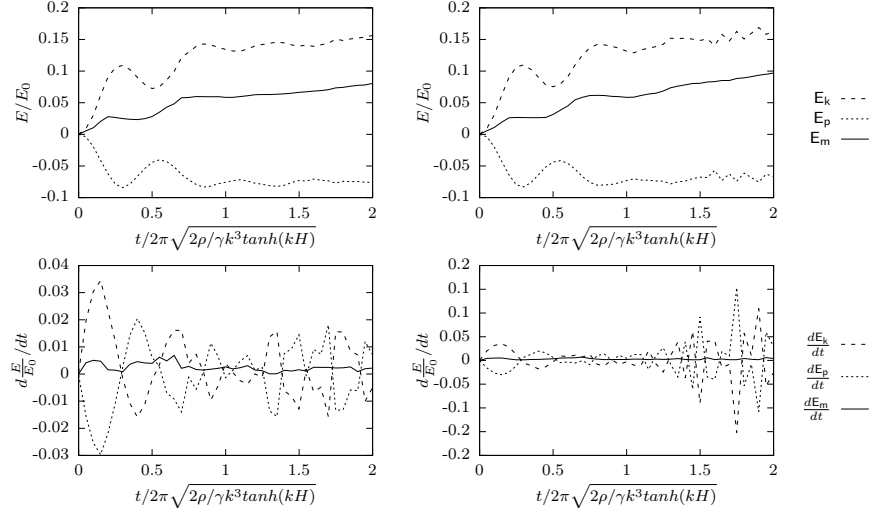


Figure 17: Energy evolution of the capillary wave with the complete Olsson and Kreiss method [11] with a single recompression stage (left), and the same method including the modified curvature interpolation (right) in a  $128 \times 128$  mesh. Top rows show the discrete values of kinetic ( $E_k$ ), potential ( $E_p$ ) and total ( $E_m$ ) energy. Bottom rows show their semi-discretized time derivative according to equations (48), (49) and (50), respectively.

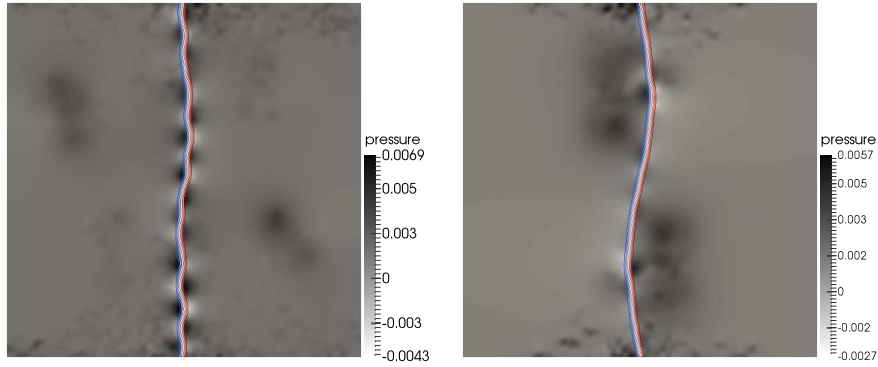


Figure 18: Pressure field and interface location at  $t = 2T$  for a capillary wave in a  $128 \times 128$  mesh advected with a single recompression step. Left figure uses the standard 2nd order shift operator while the right one uses the newly developed energy-preserving one. Contour lines are plotted for  $\Delta\theta = 0.1$ .



## 6. Concluding Remarks

By incorporating the first variation of area, equation (9), into the continuum formulation we have explicitly imposed a novel condition to the system. Equation (14) shows that the use of a smooth marker function is compatible with such a condition. This condition is implicitly incorporated into the discretized system by means of a newly developed curvature cell-to-face shift operator,  $\Upsilon$ , defined in equation (47). Analytical and numerical assessments provide evidence that, in the absence of recompression, the novel interpolation scheme preserves mechanical energy up to temporal integration by balancing kinetic and potential energy transfers to machine accuracy.

The exact value of both kinetic and potential energy is not achieved due to the lack of conservation of linear momentum. This implies that, while the transfers between surface and kinetic energy are equal and of opposite sign, its magnitude is not necessarily the correct one..

In this regard, the adoption of a fully conservative momentum formulation, along with proper discretization techniques for the convective operator, as already announced in Section 4.2, should be considered in a general case. However, the formulation of the surface tension is the most challenging term. Not being cast into a conservative form, it relies on the accurate capturing of the interface to produce a closed, and thus conservative, force field. In summary, the use of a finite grid prevents us from resolving the finest scales of the interface, represented by the marker function  $\theta$ . This under-resolution of  $\theta$ , either induced both by the mesh and the advection scheme, induces subsequent errors in the computation of both  $\hat{\eta}_i$  and  $\kappa$ , as stated by Magnini et al. [27]. These errors spread into the momentum equation, which can be seen as a back-scatter of energy from the finest, unresolved, surface representation scales into larger kinematic ones, manifesting itself as an inappropriate momentum balance, which ultimately leads to an inaccurate kinetic energy level. This is a well-known issue in multiphase flows and the object of ongoing research [48, 49].

Nevertheless, despite the lack of linear momentum conservation, mechanical energy is conserved and thus the stability of the system is guaranteed up to temporal integration. From this perspective, the novel technique may provide extra reliability

for surface energy governed phenomena, particularly those involving surface break-up or coalesce, as it may occur in atomization processes or Plateau-Rayleigh instabilities, among others.

Recompression schemes, despite producing an energetic imbalance, as has been shown in Section 5, are common in the level-set community. They preserve a coherent marker field at the expenses of introducing non-physical energy to the system. Even when the proposed method enforces the energetic consistency between marker and momentum transport equations, the inclusion of recompression prevents us from obtaining a fully energy-preserving scheme. Following the spirit described in Section 4, a first approach may be to modify the recompression step to produce not only a conservative, but an energetically neutral resharping. Enforcing a null contribution to potential energy of equation (53), if possible, would allow an arbitrary number of recompression steps, avoiding any penalty in terms of energetic balances. Although this would be desirable, it requires to re-formulate a mass- and energy- conservative recompression scheme which effectively moves the interface irrespective of advection, which is definitively not obvious.

Others have tried to include recompression within the advection step to yield a single-step method. After all, recompression is included to fix the distortion produced by interface advection. This leads to phase-field-like methods [50, 51]. Interpreting this idea as a custom-made high resolution scheme, these approaches can eventually be cast into a convective form like that in equations (46) and proceed to obtain the equivalent curvature interpolation as in equation (47). A variant of this model may be to approach the advection of the marker function as a regularization problem [52].

Lastly, both a review of the well-known symmetry-preserving scheme and the development of the energy-preserving scheme have been approached from an algebraic point of view. Aside from the advantages in terms of algebraic analysis, the use of an algebra-based discretization provides an opportunity for High Performance Computing (HPC) optimization, parallelization and portability [53]. By casting differential forms into algebraic ones, (i.e., matrices and vectors), it has been shown in [53] that nearly 90% of the operations comprised in a typical FSM algorithm for the solution of incompressible Navier-Stokes equations can be reduced to Sparse Matrix-Vector

multiplication (SpMV), generalized vector addition (AXPY) and dot product (DOT). In this regard, the present formulation falls within a smart strategy towards portable, heterogeneous, HPC.

## 7. Acknowledgements

This work has been financially supported by the Ministerio de Economía y Competitividad, Spain (ENE2017-88697-R and ENE2015-70672-P) as well as an FI AGAUR-Generalitat de Catalunya fellowship (2017FI\_B\_00616) and a Ramón y Cajal postdoctoral contract (RYC-2012-11996). The authors are grateful to Prof. Roel Verstappen, Prof. Arthur Veldman and MSc Ronald Remmerswaal for their enriching discussions.

## Appendix A. Inner products

Inner products are bilinear maps from a vector space to its base field (i.e.,  $(\cdot, \cdot)_S : S \times S \rightarrow \mathbb{K}$ ). Inner products can be defined over both continuum and discrete spaces as

$$(f, g)_S = \int_S f g dS \quad \forall f, g \in S \quad (\text{A.1})$$

This definition can be readily applied to discrete fields, yielding the definition of inner products for discrete vectors within metric spaces as

$$(\mathbf{f}_s, \mathbf{g}_s)_S = \mathbf{f}_s^T \mathbf{M}_S \mathbf{g}_s \quad (\text{A.2})$$

where  $\mathbf{M}_S$  takes over the role of integrating in space, whereas the transpose of the first element provides with the appropriate order to perform the subsequent products and sums. This can be seen by expressing  $f$  and  $g$  as a finite sum of piecewise defined base functions.

Within this framework, we can define skew-symmetry as the property of operators satisfying

$$(\phi, A\psi) = -(A\phi, \psi) \quad \forall \phi, \psi \in S \quad A : S \rightarrow S \quad (\text{A.3})$$

where, in the discrete setting,  $A$  must be a skew-symmetric matrix. Similarly, we can define duality as

$$(\phi, A\psi) = (A^*\phi, \psi) \quad \forall \phi \in S \psi \in T \quad A : T \rightarrow S \quad A^* : S \rightarrow T \quad (\text{A.4})$$

By using the aforementioned definitions and the well-known Gauss-Ostrogradsky theorem, it provides with

$$(f, \nabla \cdot \vec{g}) = \int_{\Omega} f \nabla \cdot \vec{g} = - \int_{\Omega} \nabla f \cdot \vec{g} + \int_{\partial\Omega} f \vec{g} \cdot \hat{n} \quad (\text{A.5})$$

where we can see that, assuming that there are no contributions from the boundary, the usual relation  $(f, \nabla \cdot \vec{g}) = -(\nabla f, \vec{g})$  holds as usual. However, if there is a discontinuity in either  $f$  or  $\vec{g}$  as a consequence of, say, an interface ( $\Gamma$ ) in the domain, this prevents us from using equation (A.5) directly, but rather first in both sub-domains separately and then sum them together. This results in an explicit expression as

$$(u, \nabla \cdot \vec{v}) = \int_{\Omega} u \nabla \cdot \vec{v} = \int_{\partial\Omega} u \vec{v} \cdot \hat{n} + \int_{\Gamma} [u \vec{v}] \cdot \hat{n} - \int_{\Omega} \nabla u \cdot \vec{v} \quad (\text{A.6})$$

where the discontinuity is now explicitly included in the system. Note then that for a discrete system, the aforementioned gradient-divergence duality is

$$(u_s, D\vec{v}_s)_S = -(Gu_s, \vec{v}_s)_S + \int_{\Gamma} [u_s \vec{v}_s] \quad (\text{A.7})$$

where the extra rightmost term captures the corresponding jump of the variables under consideration. Note that a proper approximation of  $\Gamma$  is required in order to obtain accurate solutions.

## References

- [1] S. Tanguy, T. Ménard, A. Berlemont, A Level Set Method for vaporizing two-phase flows, *J. Comput. Phys.* 221 (2007) 837–853.
- [2] O. Desjardins, V. Moureau, H. Pitsch, An accurate conservative level set/ghost fluid method for simulating turbulent atomization, *J. Comput. Phys.* 227 (2008) 8395–8416.
- [3] B. P. Van Poppel, O. Desjardins, J. W. Daily, A ghost fluid, level set methodology for simulating multiphase electrohydrodynamic flows with application to liquid fuel injection, *J. Comput. Phys.* 229 (2010) 7977–7996.

- [4] S. Tanguy, M. Sagan, B. Lalanne, F. Couderc, C. Colin, Benchmarks and numerical methods for the simulation of boiling flows, *J. Comput. Phys.* 264 (2014) 1–22.
- [5] M. Lepilliez, E. R. Popescu, F. Gibou, S. Tanguy, On two-phase flow solvers in irregular domains with contact line, *J. Comput. Phys.* 321 (2016) 1217–1251.
- [6] E. Gutiérrez, N. Balcázar, E. Bartrons, J. Rigola, Numerical study of Taylor bubbles rising in a stagnant liquid using a level-set/moving-mesh method, *Chem. Eng. Sci.* 164 (2017) 158–177.
- [7] C. W. Hirt, B. D. Nichols, Volume of fluid (VOF) method for the dynamics of free boundaries, *J. Comput. Phys.* 39 (1981) 201–225.
- [8] S. Osher, J. A. Sethian, Fronts propagating with curvature-dependent speed: Algorithms based on Hamilton-Jacobi formulations, *J. Comput. Phys.* 79 (1988) 12–49.
- [9] D. M. Anderson, G. B. McFadden, Diffuse-Interface Methods in fluid mechanics, *C’Est Une Rev.* (1997).
- [10] B. S. Mirjalili, S. S. Jain, M. S. Dodd, Interface-capturing methods for two-phase flows : An overview and recent developments, *Annu. Res. Briefs* (2017) 117–135.
- [11] E. Olsson, G. Kreiss, A conservative level set method for two phase flow, *J. Comput. Phys.* 210 (2005) 225–246.
- [12] E. Olsson, G. Kreiss, S. Zahedi, A conservative level set method for two phase flow II, *J. Comput. Phys.* 225 (2007) 785–807.
- [13] N. Balcázar, L. Jofre, O. Lehmkuhl, J. Castro, J. Rigola, A finite-volume/level-set method for simulating two-phase flows on unstructured grids, *Int. J. Multiph. Flow* 64 (2014) 55–72.
- [14] A. J. Chorin, Numerical solution of the Navier-Stokes equations, *Math. Comput.* 22 (1968) 745–762.

- [15] R. Verstappen, A. Veldman, Direct numerical simulation of turbulence at lower costs, *J. Eng. Math.* (1997) 143–159.
- [16] R. Verstappen, A. Veldman, Symmetry-preserving discretization of turbulent flow, *J. Comput. Phys.* 187 (2003) 343–368.
- [17] K. Lipnikov, G. Manzini, M. Shashkov, Mimetic finite difference method, *J. Comput. Phys.* 257 (2014) 1163–1227.
- [18] N. Robidoux, S. Steinberg, A discrete vector calculus in tensor grids, *Comput. Methods Appl. Math.* 11 (2011) 23–66.
- [19] E. Tonti, Why starting from differential equations for computational physics?, *J. Comput. Phys.* 257 (2014) 1260–1290.
- [20] J. B. Perot, Discrete Conservation Properties of Unstructured Mesh Schemes, *Annu. Rev. Fluid Mech.* 43 (2011) 299–318.
- [21] F. X. Trias, A. Gorobets, A. Oliva, Turbulent flow around a square cylinder at Reynolds number 22,000: A DNS study, *Comput. Fluids* 123 (2015) 87–98.
- [22] L. Paniagua, O. Lehmkuhl, C. Oliet, C. D. Pérez-Segarra, Large eddy simulations (LES) on the flow and heat transfer in a wall-bounded pin matrix, *Numer. Heat Transf. Part B Fundam.* 65 (2014) 103–128.
- [23] H. Giráldez, C. D. Pérez Segarra, C. Oliet, A. Oliva, Heat and moisture insulation by means of air curtains: Application to refrigerated chambers, *Int. J. Refrig.* 68 (2016) 1–14.
- [24] D. Fuster, An energy preserving formulation for the simulation of multiphase turbulent flows, *J. Comput. Phys.* 235 (2013) 114–128.
- [25] M. Sussman, K. M. Smith, M. Y. Hussaini, M. Ohta, R. Zhi-Wei, A sharp interface method for incompressible two-phase flows, *J. Comput. Phys.* 221 (2007) 469–505.

- [26] B. Lalanne, L. R. Villegas, S. Tanguy, F. Risso, On the computation of viscous terms for incompressible two-phase flows with Level Set/Ghost Fluid Method, *J. Comput. Phys.* 301 (2015) 289–307.
- [27] M. Magnini, B. Pulvirenti, J. R. Thome, Characterization of the velocity fields generated by flow initialization in the CFD simulation of multiphase flows, *Appl. Math. Model.* 40 (2016) 6811–6830.
- [28] D. Jacqmin, Calculation of Two-Phase Navier–Stokes Flows Using Phase-Field Modeling, *J. Comput. Phys.* 155 (1999) 96–127.
- [29] D. Jamet, D. Torres, J. U. Brackbill, On the Theory and Computation of Surface Tension: The Elimination of Parasitic Currents through Energy Conservation in the Second-Gradient Method, *J. Comput. Phys.* 182 (2002) 262–276.
- [30] D. Jamet, C. Misbah, Toward a thermodynamically consistent picture of the phase-field model of vesicles: Curvature energy, *Phys. Rev. E - Stat. Nonlinear, Soft Matter Phys.* 78 (2008) 1–8.
- [31] G. Tryggvason, B. Bunner, a. Esmaeeli, D. Juric, N. Al-Rawahi, W. Tauber, J. Han, S. Nas, Y.-J. Jan, A Front-Tracking Method for the Computations of Multiphase Flow, *J. Comput. Phys.* 169 (2001) 708–759.
- [32] M. Sussman, P. Smereka, S. Osher, A Level Set Approach for Computing Solutions to Incompressible Two-Phase Flow, *J. Comput. Phys.* 114 (1994) 146–159.
- [33] S. Chen, B. Merriman, S. Osher, P. Smereka, A Simple Level Set Method for Solving Stefan Problems, *J. Comput. Phys.* 135 (1997) 8–29.
- [34] T. Waławczyk, A consistent solution of the re-initialization equation in the conservative level-set method, *J. Comput. Phys.* 299 (2015) 487–525.
- [35] J. Brackbill, D. Kothe, C. Zemach, A continuum method for modeling surface tension, *J. Comput. Phys.* 100 (1992) 335–354.

- [36] T. Frankel, *The Geometry of Physics*, 3 ed., Cambridge University Press, Cambridge, 2012. URL: <http://ebooks.cambridge.org/ref/id/CB09781139061377>. doi:10.1017/CB09781139061377.
- [37] J. E. Hicken, F. E. Ham, J. Militzer, M. Koksal, A shift transformation for fully conservative methods: Turbulence simulation on complex, unstructured grids, *J. Comput. Phys.* 208 (2005) 704–734.
- [38] F. X. Trias, O. Lehmkuhl, A. Oliva, C. D. Pérez-Segarra, R. W. C. P. Verstappen, Symmetry-preserving discretization of Navier-Stokes equations on collocated unstructured grids, *J. Comput. Phys.* 258 (2014) 246–267.
- [39] F. Capuano, G. Coppola, L. Rández, L. de Luca, Explicit Runge–Kutta schemes for incompressible flow with improved energy-conservation properties, *J. Comput. Phys.* 328 (2017) 86–94.
- [40] J. T. Davies, E. K. Rideal, *Interfacial Phenomena*, Academic Press Inc., London, 1961. doi:10.1016/B978-0-12-206056-4.X5001-2.
- [41] W. Rozema, J. C. Kok, R. W. Verstappen, A. E. Veldman, A symmetry-preserving discretisation and regularisation model for compressible flow with application to turbulent channel flow, *J. Turbul.* 15 (2014) 386–410.
- [42] N. Valle, X. Álvarez, F. X. Trias, J. Castro, A. Oliva, Algebraic implementation of a flux limiter for heterogeneous computing, in: *Tenth Int. Conf. Comput. Fluid Dyn.*, Barcelona, July, 2018.
- [43] J. K. Patel, G. Natarajan, A generic framework for design of interface capturing schemes for multi-fluid flows, *Comput. Fluids* 106 (2015) 108–118.
- [44] O. Ubbink, R. Issa, A Method for Capturing Sharp Fluid Interfaces on Arbitrary Meshes, *J. Comput. Phys.* 153 (1999) 26–50.
- [45] S. H. Lamb, *Hydrodynamics*, Dover Publications, Inc., New York, NY, 1945.
- [46] D. Fyfe, E. Oran, M. Fritts, Surface tension and viscosity with lagrangian hydrodynamics on a triangular mesh, *J. Comput. Phys.* 76 (1988) 349–384.



- [47] S. Popinet, Numerical Models of Surface Tension, *Annu. Rev. Fluid Mech.* 50 (2017) 49–75.
- [48] J. Kim, A continuous surface tension force formulation for diffuse-interface models, *J. Comput. Phys.* 204 (2005) 784–804.
- [49] M. O. Abu-Al-Saud, S. Popinet, H. A. Tchelepi, A conservative and well-balanced surface tension model, *J. Comput. Phys.* 371 (2018) 896–913.
- [50] J. L. Guermond, M. Q. de Luna, T. Thompson, An conservative anti-diffusion technique for the level set method, *J. Comput. Appl. Math.* 321 (2017) 448–468.
- [51] S. Mirjalili, C. B. Ivey, A. Mani, A conservative diffuse interface method for two-phase flows with provable boundedness properties (2018).
- [52] F. X. Trias, D. Folch, A. Gorobets, A. Oliva, Spectrally-Consistent Regularization of Navier–Stokes Equations, *J. Sci. Comput.* (published online) (2018).
- [53] X. Álvarez, A. Gorobets, F. X. Trias, R. Borrell, G. Oyarzun, HPC2—A fully-portable, algebra-based framework for heterogeneous computing. Application to CFD, *Comput. Fluids* 173 (2018) 285–292.